CrystEngComm

ROYAL SOCIETY OF CHEMISTRY

PAPER

View Article Online
View Journal | View Issue

Check for updates

Cite this: *CrystEngComm*, 2026, **28**, 255

Mechanochemical synthesis and micro-electron diffraction analysis of rare earth–aminopolycarboxylate coordination compounds

Ecem Çelik,[a] Pierre Le Magueres,[b] Eric W. Reinheimer,[b] Korey P. Carter *[a] and Tori Z. Forbes *[a]

Mechanochemical synthesis offers synthetic pathways to new materials that are inaccessible *via* traditional solvent-based approaches. In this work, we evaluated how mechanochemical synthetic variables (*e.g.* time, frequency, liquid assisted grinding (LAG), metal precursors) impacted the products obtained from reactions containing La(III) and ethylenediaminetetraacetic acid (EDTA). We found that tuning mechanochemical parameters (*i.e.*, time and frequency) affected reactivity and use of different La(III) salt precursors (La_2O_3, $LaCl_3{\cdot}7H_2O$, $LaPO_4{\cdot}xH_2O$, $La(NO_3)_3{\cdot}6H_2O$, and $La(OOCCH_3)_3{\cdot}1.5H_2O$) led to variations in solid-state products. Reactivity trends were largely consistent with trends in the relative lattice energies of the lanthanum starting materials, with the outlier (La_2O_3) potentially undergoing additional hydroxylation on particle surfaces during LAG. Two products were successfully isolated and structurally characterized using electron diffraction, including a 1-D chain and a 2-D sheet prepared from La_2O_3 (**LaEDTA1**) and $LaCl_3{\cdot}7H_2O$ (**LaEDTA2**), respectively. Detailed structural analysis revealed protonation sites on EDTA ligands that contribute to overall charge neutrality of both compounds. Infrared spectroscopy further confirmed ligand protonation in **LaEDTA1** and **LaEDTA2**, while thermogravimetric and elemental analysis measurements provided complementary characterization information. Finally, field emission scanning electron microscopy results confirmed the elemental compositions of both products, with trace levels of iron observed that likely originate from stainless-steel milling media.

Received 26th September 2025,
Accepted 23rd November 2025

DOI: 10.1039/d5ce00935a

rsc.li/crystengcomm

Open Access Article. Published on 24 November 2025. Downloaded on 2/15/2026 9:04:38 AM.
This article is licensed under a Creative Commons Attribution 3.0 Unported Licence.

1. Introduction

The rational design of hybrid materials, such as coordination polymers (CPs), starts with the formation of metal ligand complexes in solution.[1,2] The assembly of one-, two-, and three-dimensional hybrid materials affects their structure and properties, and metal coordination preferences and ligand flexibility are known to play crucial roles in determining network dimensionality.[3,4] Typically, metal–ligand interactions in solution are governed by binding energies and pH conditions, as well as reaction conditions such as solubility, precursor selection, identity of co-solutes, temperature, and solvent composition, which influence precipitation of solid-state materials and resulting structural topologies.[5,6] Synthesis of crystalline hybrid materials has historically relied on solution-based techniques, such as hydrothermal and solvothermal methods, where reactions are governed by solvent properties and the amount of thermal energy added.[2] While these methods have been widely successful in producing highly crystalline molecular and extended structures, they also come with limitations such as prolonged reaction times, high energy inputs, lower yields, and bulk solvent use, making them less efficient and difficult to scale for wider applications.[2] Solution-based synthesis also typically favors the formation of thermodynamically stable phases,[7] so alternative synthetic techniques that minimize solvent dependency, reduce reaction times and harsh conditions, and enable access to a wider synthetic chemical space are highly desirable.[8,9]

Mechanochemistry has emerged as a powerful synthetic approach for synthesizing hybrid materials[10–14] that offers solvent-minimized and energy efficient pathways to metal–ligand assembly.[15–17] Unlike traditional solution-based methods, mechanochemical reactions occur in the solid state and are driven by mechanical forces, such as grinding or milling, which promote direct interactions between reactants, enabling rapid synthesis and complexation under ambient or mild conditions that can be more difficult to achieve in solutions.[16,18,19] Mechanochemical synthesis can be performed under various conditions such as using a reactive atmosphere (reactive ball milling (BM)), a cryogenic setting, or liquid-assisted grinding (LAG). Among them, LAG stands out as a promising route where

[a] *Department of Chemistry, University of Iowa, Iowa City, IA 52242, USA. E-mail: korey-carter@uiowa.edu, tori-forbes@uiowa.edu*
[b] *Rigaku Americas Corp, The Woodlands, TX 77381, USA*

Open Access Article. Published on 24 November 2025. Downloaded on 2/15/2026 9:04:38 AM. This article is licensed under a Creative Commons Attribution 3.0 Unported Licence.

a small amount of solvent is introduced during milling to enhance reactivity in metal complexation reactions, while maintaining the benefits of mechanochemical synthesis.[20–25] Moreover, mechanochemical synthesis allows for more synthetic versatility by enabling control over key experimental parameters, including milling time, ball-to-powder weight ratio, and grinding frequency. By adjusting these parameters, it is possible to tailor reaction pathways and influence the characteristics of final products.[26] Mechanochemistry has been widely applied in organic[27–30] and main group metal–organic chemistry,[17,31–33] and more recently has received renewed research interest in f-block systems. For example, Fetrow *et al.* demonstrated the synthesis of rare earth phosphinodiborates in only 15 minutes,[34] while Kravchuk *et al.* showed that UO_3 can be rapidly converted into U(VI) triperoxide materials by grinding with solid peroxides within 15–30 minutes.[35] Extending these advances, Kravchuk *et al.* further demonstrated that U(IV)O_2 undergoes mechanochemical oxidation with alkali peroxides (Li_2O_2, Na_2O_2) under LAG to yield crystalline U(VI) triperoxide phases within 30 minutes.[36] Depending on the conditions used, mechanochemical synthesis can yield a variety of structural phases, including compounds that are structurally distinct from those obtained *via* conventional routes.[37,38] This flexibility also enables greater synthetic tunability, which is particularly relevant for hybrid materials, where ligand coordination can play a key role in determining structural dimensionality and resulting material properties.

Mechanochemical reactions have also been shown to facilitate the formation of hybrid materials, promoting extended frameworks with desired dimensionalities;[39–41] however, less is known about metal–ligand binding in mechanochemical reactions featuring organic molecules with strong chelating abilities, wherein metal chelation effects may compete with extended network formation. Aminopolycarboxylate (APC) ligands, such as ethylenediaminetetraacetic acid (EDTA), are a class of ligands of particular relevance due to their strong metal chelating ability and use as aqueous holdback agents in RE separations.[42–48] EDTA, $[CH_2N(CH_2COOH)_2]_2$, is a tetrabasic acid that has been widely studied in coordination chemistry,[49] which is known for forming highly stable complexes with rare earth elements (REEs).[50–52] EDTA has also been used as a chelator in solvent assisted mechanochemical extractions of REEs from alternative material sources such as end-of-life fluorescent lamps and coal fly ash.[53,54] The coordinative flexibility of EDTA, made possible by its multiple nitrogen and oxygen donor sites, as well as the various coordination numbers accessible to rare-earth cations leads to variability in the dimensionality of RE–EDTA hybrid materials under different synthetic conditions.[55,56] For instance, in solution, EDTA predominantly favors molecular complexation;[57,58] however, when the temperatures and pressures are increased during hydrothermal synthesis, EDTA has also been shown to promote the formation of extended metal–ligand networks, suggesting that synthetic conditions dictate the extent of metal-ion complexation and the resulting structural properties.[59] Unlike hydrothermal reactions, which are driven by thermal energy and changes in pressure that alter solvent properties, the direct mechanical energy inputs in mechanochemistry activate bonding by inducing local high pressures and temperatures and force mixing of reactants. Currently, it is unclear how solubility-, thermal energy-, and mechanically driven synthetic pathways influence the final structural and topological features in APC materials.

Herein we used the La(III)–EDTA system as a platform to investigate how mechanochemical conditions influence the structure and assembly of RE-APC materials. Lanthanum (La) was selected as a representative REE due to its large ionic radius, flexible coordination environment, and diamagnetic, non-luminescent electronic configuration, which allowed for structural and reactivity studies without the complicating optical or magnetic effects observed in other lanthanides. The ability of La^{3+} to adopt high coordination numbers and support extended frameworks is well established in its citrate and carboxylate complexes.[60–62] Furthermore, it exhibits comparable chelation behavior to other lanthanides in aminopolycarboxylate systems, such as EDTA, making it an effective model for probing RE–APC complexation studies under mechanochemical conditions.[63–65] In addition, given its structural versatility[42,64,67,68] and relevance to separations chemistry[66,69] and catalysis,[70] La^{3+} provides a suitable platform for understanding rare-earth coordination behavior in the solid-state synthetic environments. We evaluated how different La(III) salt precursors (La_2O_3, $LaCl_3{\cdot}7H_2O$, $LaPO_4{\cdot}xH_2O$, $La(NO_3)_3{\cdot}6H_2O$, and $La(OOCCH_3)_3{\cdot}1.5H_2O$) and tuning of mechanochemical parameters (*i.e.*, liquid assisted grinding (LAG), time, and frequency) impacted the reactivity and resulting solid-state products using powder X-ray diffraction (PXRD). From the La_2O_3 and $LaCl_3{\cdot}7H_2O$ systems, two solid state products (**La-EDTA1** and **La-EDTA2**, respectively) were characterized by electron diffraction (MicroED), vibrational spectroscopy, thermogravimetric analysis (TGA), combustion elemental analysis (EA), and field emission scanning electron microscopy (FE-SEM). Structural characterization by MicroED revealed the formation of extended structural topologies, consistent with recent reports in literature where electron diffraction was employed to resolve coordination frameworks from submicron or nanocrystalline materials obtained *via* mechanochemical synthesis,[41,71] and chemical characterization of the bulk products was used to determine purity, chemical composition, and overall thermal stability.

2. Experimental

2.1 Materials

Mechanochemical LAG reactions were conducted using rare earth salts including lanthanum(III) chloride heptahydrate (Beantown Chemical, Inc., 99.99%), lanthanum(III) oxide (Thermo Scientific Inc., 99.99%), lanthanum(III) phosphate hydrate (Thermo Scientific Inc., 99.99%), lanthanum(III) nitrate hexahydrate (Beantown Chemical, Inc., 99.99%), lanthanum(III) acetate sesquihydrate (Thermo Scientific Inc., 99.99%), and ethylenediaminetetraacetic acid (EDTA) (Alfa Aesar Inc., 99%). All reagents are commercially available and were used without further purification. All LAG reactions

 This journal is © The Royal Society of Chemistry 2026

Open Access Article. Published on 24 November 2025. Downloaded on 2/15/2026 9:04:38 AM. This article is licensed under a Creative Commons Attribution 3.0 Unported Licence.

used ultrapure Millipore water (18.2 MΩ) obtained from a Milli-Q IQ 7000 purification system.

2.2 Mechanochemical synthesis

Mechanochemical LAG synthesis for La(III)–EDTA compounds was performed using a Retsch MM500 Vario Mixer Mill with a 5 mL stainless steel milling jar containing four 5 mm stainless steel milling balls (304 grade). All reactions were conducted using a 1 : 2 molar ratio of La(III) salts (La_2O_3, $LaCl_3{\cdot}7H_2O$, $LaPO_4{\cdot}xH_2O$, $La(NO_3)_3{\cdot}6H_2O$, and $La(OOCCH_3)_3{\cdot}1.5H_2O$) to EDTA and followed LAG protocols with the addition of 100 μL of ultrapure Millipore water (18.2 MΩ), corresponding to $\eta \approx 1$ μL mg^{-1}. The grinding jars were sealed and inserted into a Retsch MM500 Vario Mixer Mill operating at frequencies ranging from 15–30 Hz for varying durations (*i.e.*, 15–30 minutes) with reaction conditions considered optimized, for each La(III) precursor, once crystalline material peaks appeared in PXRD patterns and no further changes were observed when longer milling times were used. The reaction between La_2O_3 and EDTA was performed at 30 Hz for 30 minutes, whereas $LaCl_3{\cdot}7H_2O$ and EDTA were milled at 25 Hz for 15 minutes. Similarly, the reactions of $LaPO_4{\cdot}xH_2O$, $La(NO_3)_3{\cdot}6H_2O$, and $La(OOCCH_3)_3{\cdot}1.5H_2O$ with EDTA were conducted at 15 Hz for 15 minutes, 15 Hz for 15 minutes, and 30 Hz for 30 minutes, respectively. After milling, all reaction mixtures were slightly wet; thus, the solid products were dried overnight under ambient conditions. The jars were then opened on the bench, and the powders were carefully transferred to sample vials. Any remaining material was recovered by gently scraping the jar walls and milling balls with a clean spatula. No solvent was used during recovery, and all final products were stored in scintillation vials as fine powders for further analysis. Schemes describing the synthetic details for the two representative compounds, **LaEDTA1**, ($[La(C_{10}H_{13}N_2O_8)H_2O]$), and **LaEDTA2**, ($[La_2(C_{10}H_{14}N_2O_8)Cl_2(H_2O)_6]Cl_2$), can be found in Fig. S1, SI. Similar solution-based reactions were performed for LaEDTA1 and LaEDTA2 where the same conditions were exposed to aqueous solutions and the resulting products were further characterized to identify the product.

2.3 Powder X-ray diffraction

Formation of crystalline product within the synthesized materials was verified through powder X-ray diffraction (PXRD) analysis using a Bruker D8 Advance diffractometer equipped with Ni-filtered Cu Kα radiation (λ = 1.5418 Å). Samples were dried and ground to fine powders using a mortar and pestle and analyzed using zero background silica sample holders. Data were collected at an operating voltage of 40 kV and current of 40 mA, in continuous mode with a scan range of 3–60° (2θ) and a step size of 0.02°. Processing of PXRD patterns, background subtraction, smoothing, $K_{\alpha 2}$ stripping, and peak selection was done using PreDICT indexing software from the International Centre for Diffraction Data (ICDD).[72] The obtained diffraction patterns were compared with simulated patterns generated from crystallographic information files (CIFs) using CrystalDiffract software within the CrystalMaker software package,[73] while bulk phase purity was evaluated using the JADE software package.[74]

2.4 Electron diffraction

Mechanochemical reactions did not yield crystals that were suitable large enough for analysis *via* single crystal X-ray diffraction (SC-XRD); thus, electron diffraction was used for these measurements. Samples were ground to fine powders using a mortar and pestle and a portion of the powder material was gently crushed between two glass slides to make the crystals suitably thin for Micro-ED studies. A 3 mm Cu TEM grid with continuous carbon film was dropped into the powder to gather crystallites and shaken to shed some of the powder and obtain a grid with sparsely spread crystallites. The grid was then placed into a Gatan Elsa sample cryo-holder model 698, and the sample was cooled down to 100 K, using a Gatan transfer station. Finally, the cryo-holder was inserted into the XtaLAB Synergy-ED.

MicroED measurements were performed using a Rigaku XtalAB Synergy-ED equipped with a JEOL 200 kV electron source, column and beam optics and a Rigaku HyPix-ED detector, all optimized for operation in the MicroED experimental setup.[75] The electron beam has a wavelength of 0.0251 Å and runs in a high vacuum of about 1.5×10^{-7} torr. Partial datasets were collected rapidly on several individual crystallites, using the continuous rotation method, and processed concurrently, all in the Rigaku program CrysAlisPro-ED.[76] Two to three data sets were then merged to improve completeness. Statistics on both the individual and the merged data sets are shown in the SI section, along with pictures of the crystallites used for data collection and examples of their diffraction patterns.

The crystal structures for both compounds were readily solved with the ShelXT[77] structure solution program within the AutoChem[78] interface, an automated version of Olex2,[79] using intrinsic phasing. The model was kinematically refined with the ShelXL[80] refinement package, using least squares minimization, with all non-H atoms refined anisotropically. Atomic electron scattering factors for the relevant chemical elements were applied in the .ins file for solution and refinement. All figures for compounds **LaEDTA1** and **LaEDTA2** were made using CrystalMaker.[73] Crystallographic parameters and structural refinement details are located in Table S2, SI.

2.5 Additional chemical characterization

Infrared (IR) spectra were collected for all La(III)–EDTA solid-state products using a Bruker VERTEX 70v FTIR spectrometer, equipped with a platinum ATR microscope objective, and data were processed using the OPUS 8.5 software package. Data were recorded over the 4000–400 cm^{-1} range with a resolution of 0.4 cm^{-1}. Spectral fitting of all IR spectra was done in Origin 2025 software using Voigt lineshapes.

Open Access Article. Published on 24 November 2025. Downloaded on 2/15/2026 9:04:38 AM. This article is licensed under a Creative Commons Attribution 3.0 Unported Licence.

LaEDTA1 and **LaEDTA2** were analyzed with a TA Instruments SDT-Q600 thermogravimetric analyzer (TGA)/differential scanning calorimeter (DSC). Approximately 5 mg of each compound was placed on the instrument and a nitrogen carrier gas with a flow rate of 50.0 mL min^{-1} was used during analysis. The samples were heated from 323–1073 K with ramp rate of 10 °C min^{-1} and both weight loss and heat flow were measured *via* TGA/DSC. Final products after TGA/DSC measurements were La_2O_3 as well as minor phases that could not be identified *via* PXRD analysis.

Elemental analysis of **LaEDTA1** and **LaEDTA2** was performed to further confirm material bulk purity. Approximately 1.5–3 mg of each sample was weighed in duplicate using a Mettler Toledo microbalance with 1 μg accuracy. Subsequently, samples were placed in tin capsules, crimped to form a small pellet, and then combustion analysis was initiated using an Exeter Analytical CE440 combustion CHN elemental analyzer.

The elemental composition of each sample was verified using energy dispersive spectroscopy with a JEOL JSM-1T700HR field emission scanning electron microscope. The mechanochemically synthesized **LaEDTA1** and **LaEDTA2** were adhered to SEM stubs using double-sided carbon tape and gold tape, respectively, and the operating voltage and the emission current were 2.5 kV and 80–120 μA.

3. Results and discussion

3.1 Mechanochemical synthesis optimization and product formation

A range of physical variables (time, frequency) and metal-to-ligand ratios were evaluated to determine the optimal synthetic conditions for obtaining La(III)–EDTA solid products from mechanochemical reactions. A summary of all La(III) precursors examined under optimized milling conditions and their corresponding reaction outcomes is provided in Table S1, SI. Initially, a 1 : 1 metal-to-ligand ratio was evaluated, but the PXRD analysis revealed amorphous products with no distinct crystalline features. When the metal-to-ligand ratio was increased to 1 : 2, the reaction successfully yielded crystalline materials. Time-dependent studies showed that for $LaCl_3{\cdot}7H_2O$–EDTA, crystalline materials were obtained after 15 minutes of milling at 25 Hz, and extending milling time beyond 15 minutes either yielded no significant changes in PXRD patterns or the formation of amorphous materials (Fig. S4, SI). In the case of EDTA with $LaPO_4{\cdot}xH_2O$ or $La(NO_3)_3{\cdot}6H_2O$ precursors, 15 minutes of milling with EDTA yielded the same results as longer milling times and frequencies. In contrast, the complexation of La_2O_3 with EDTA required 30 minutes of milling at 30 Hz to produce new crystalline material and these parameters were selected as the optimized milling conditions. $La(OOCCH_3)_3{\cdot}1.5H_2O$ also required a longer milling time of 30 minutes to yield any additional crystalline phases, as 15 minutes was insufficient to promote a reaction between the starting materials. Milling times were therefore adjusted according to the reactivity of the starting lanthanum salt, with preference given to shorter times when crystalline products could be obtained. Milling frequency also significantly impacted product crystallinity. An initial frequency of 15 Hz produced largely amorphous materials, except in the reactions featuring $LaPO_4{\cdot}xH_2O$ and $La(NO_3)_3{\cdot}6H_2O$, where crystalline starting materials were maintained even when the milling frequency was increased indicating no change in reactivity. Increasing the frequency to 25 Hz for the $LaCl_3{\cdot}7H_2O$ reaction also resulted in crystalline material, while the reactions with La_2O_3 and $La(OOCCH_3)_3{\cdot}1.5H_2O$ required 30 Hz to achieve crystalline materials.

Next, our efforts to optimize the mechanochemical synthesis of La(III)–EDTA compounds evaluated the impact of neat grinding *versus* LAG on the formation of solid products. Overall, neat grinding of La_2O_3 with EDTA did not produce new crystalline phases relative to the starting materials, consistent with the general low reactivity of oxides. In contrast, milling $LaCl_3{\cdot}7H_2O$ with EDTA yielded the same crystalline material regardless of whether liquid-assisted grinding was employed or not (Fig. S5 and S6, SI). Introducing 100 μL of ultrapure Milli-Q water (η = 1) during milling, specifically in the case of $LaCl_3{\cdot}7H_2O$ and La_2O_3 with EDTA, facilitated metal-ion complexation and yielded crystalline hybrid materials, resulting in well-defined diffraction peaks. The presence of small amounts of water likely enhances reactivity, allowing for increased interactions between La(III) precursors and EDTA, thereby enabling structural rearrangement and formation of new phases. As a result, LAG with η = 1 was used for all optimized mechanochemical reactions in this series.

Of the chemical variables that were considered, the identity of the lanthanum starting material had a significant impact on the resulting phase formation, as indicated by the PXRD patterns of the solid products. Use of $LaPO_4{\cdot}xH_2O$ as the lanthanum starting material did not result in significant reactivity as the diffractogram of the product only contains evidence of the starting materials (Fig. 1A). In the case of lanthanum acetate, the powder pattern of the resulting mechanochemical product primarily contained features consistent with the presence of EDTA, with only a small peak at ~24° 2θ suggesting a small amount of new product may have formed (Fig. 1B). Changing the lanthanum precursor to $La(NO_3)_3{\cdot}6H_2O$ did lead to partial reactivity as evidenced by the in-growth of new peaks at 11.69, 18.36, 21.69, and 25.15° 2θ (Fig. 1C). Under optimized conditions, the reaction between La_2O_3 and EDTA, milled at 30 Hz for 30 minutes, exhibited a PXRD pattern with well-defined peaks that were significantly different from both reactants (Fig. 1D). Similarly, the reaction between $LaCl_3{\cdot}7H_2O$ and EDTA, milled at 25 Hz for 15 minutes, yielded a product with a distinct PXRD pattern compared to its starting materials, suggesting the formation of a structurally different phase (Fig. 1E).

The formation of new products from mechanochemical reactions with different metal precursors is driven by both chemical and physical characteristics of the reaction mixture. Similar to solution-based chemistry, the reaction thermodynamics of a mechanochemical reaction are impacted

 This journal is © The Royal Society of Chemistry 2026

Open Access Article. Published on 24 November 2025. Downloaded on 2/15/2026 9:04:38 AM. This article is licensed under a Creative Commons Attribution 3.0 Unported Licence.

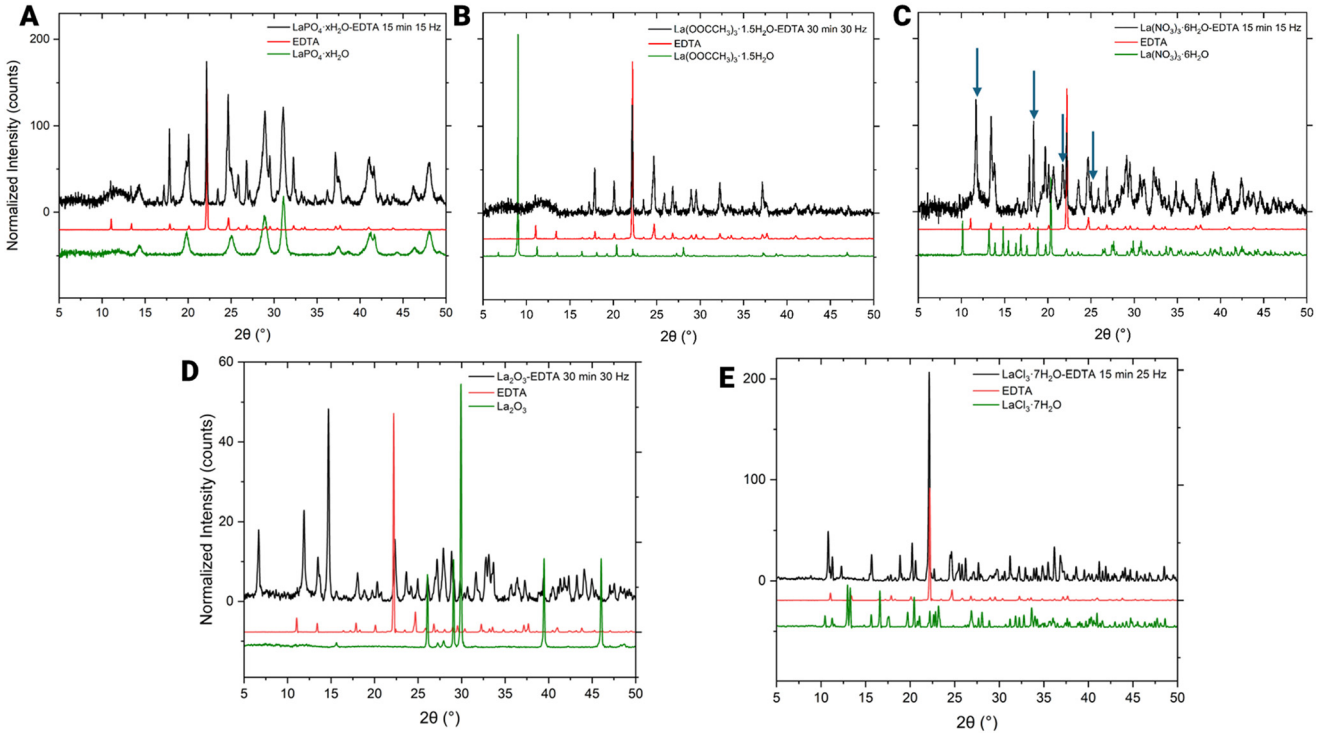

Fig. 1 Powder X-ray diffraction patterns for the lanthanum reagent (green trace), EDTA salt (red trace), and the resulting product after mechanochemical reactions (black trace) for (A) $LaPO_4{\cdot}xH_2O$, (B) $La(OOCCH_3)_3{\cdot}1.5H_2O$, (C) $La(NO_3)_3{\cdot}6H_2O$, (D) La_2O_3, and (E) $LaCl_3{\cdot}7H_2O$ starting materials.

by the starting materials, which can govern the overall changes in formation enthalpy of the product. In addition, there are activation barriers for the reaction that must be overcome to facilitate product formation, and previous mechanochemistry research has noted that different grinding frequencies can be linked to overcoming these barriers.[81] The use of liquid assisted grinding can also affect chemical reactivity as the addition of small amounts of liquid enhances molecular mobility at particle interfaces and introduces catalytic and templating effects, thereby lowering activation energy barriers and influencing binding kinetics.[82] However, unlike solution-based methods, there are also physical aspects that need to be considered as well. Starting material hardness may also impact the overall reactivity because it can influence the particle size and surface area available for reactions to occur. Therefore, higher lattice energies, which indicate the amount of energy required to break bonds in a solid-state material, directly correlate with increased hardness, and this is a key criterion to consider when evaluating bond breaking processes within mechanochemical reactions.

The variance in reactivity observed among the lanthanum precursors can be systematically understood by examining their respective lattice energies. As such, an inverse relationship exists between the lattice energy of a compound and its susceptibility to mechanochemical transformation; materials with lower lattice energies exhibit weaker lattice cohesion and are therefore more reactive under applied mechanical forces. This principle elucidates the observed reactivity trend herein, wherein the precursor with the highest lattice energy, lanthanum phosphate, was minimally reactive under all mechanochemical conditions, with no noticeable decrease in the crystallinity. This finding is consistent with its predicted high lattice energy (~5500 kJ mol^{-1}) arising from the large electrostatic forces between the La^{3+} and PO_4^{3-} ions. In contrast, lanthanum chloride was the most reactive species, a behavior attributed to its comparatively low lattice energy of approximately 4263 kJ mol^{-1}. The intermediate reactivities of lanthanum acetate and lanthanum nitrate also align with this principle, as their lattice energies are predicted to be slightly higher than that of lanthanum chloride. However, lanthanum oxide is an outlier in this trend, as the material is relatively hard[83] and exhibits high thermal stability, yet displays clear reactivity, despite its intrinsically high lattice energy of ~12 452 kJ mol^{-1}.[20,84] This observation can be explained by an *in situ* chemical transformation due to the hydroxylation of the particle surface, since La_2O_3 is highly hygroscopic.[85] During LAG, the oxide likely reacts with water (supported by IR spectroscopy, *vide infra*) to form a surface layer of lanthanum hydroxide. This species, $La(OH)_3$, possesses a much lower lattice energy of ~4443 kJ mol^{-1}, making it significantly more susceptible to reaction than the parent oxide. Therefore, the use of LAG can enhance the ability of La_2O_3 to react with EDTA in ways that were not accessible for the pristine oxide starting material in a neat reaction (Fig. S5, SI). This result further highlights the potential for mechanochemical methods to facilitate the reaction of unreactive precursors such as metal oxides within a short period of time.[86]

Open Access Article. Published on 24 November 2025. Downloaded on 2/15/2026 9:04:38 AM. This article is licensed under a Creative Commons Attribution 3.0 Unported Licence.

3.2 Characterization of the mechanochemical products LaEDTA1 and LaEDTA2

Electron Diffraction (ED). Among all reactions studied, the La_2O_3–EDTA (**LaEDTA1**) and $LaCl_3{\cdot}7H_2O$–EDTA (**LaEDTA2**) reactions were selected for further structural analysis using electron diffraction (ED). These two reactions were prioritized because their PXRD patterns exhibited the most distinct Bragg peak shifts and intensity changes compared to their starting materials, suggesting substantial structural reorganization in the solid-state. Initial searches of the ICDD PDF-4+ database did not yield a match to these phases, which indicated they may be unknown materials. Therefore, electron diffraction studies were performed to elucidate the structural characteristics of the **LaEDTA1** and **LaEDTA2** products.

Structural characterization of **LaEDTA1** revealed the formation of a previously reported 1-D chain topology,[59] but our analysis provided additional information on the specific location of the protonation site within the EDTA linker. As with the previous analysis by X-ray diffraction, ED analysis of **LaEDTA1** showed that the extended solid is linked through the EDTA ligand to form a compound with the overall formula $[La(C_{10}H_{13}N_2O_8)H_2O]$. The single unique La(III) metal center features a coordination number of nine and adopts a tricapped trigonal prismatic molecular geometry, a well-known motif in lanthanide–aminopolycarboxylate coordination chemistry obtained *via* solution-based methods.[87–89] The coordination sphere around the La(III) center consists of one aqua ligand, two bridging carboxylate oxo groups, and a triply deprotonated EDTA ligand, which chelates the La(III) atom through both nitrogen and carboxylate oxygen donor atoms (Fig. 2A). Bond distances and angles observed within **LaEDTA1** are similar to the previously reported compound (Table S3, SI), and La–O bond distances range from 2.43(2) Å to 2.616(19) Å.[68] Notably, the bridging La–O bonds (La1–O1: 2.523(18) Å, La1–O5: 2.514(18) Å) are slightly longer than the chelating La–O bonds,

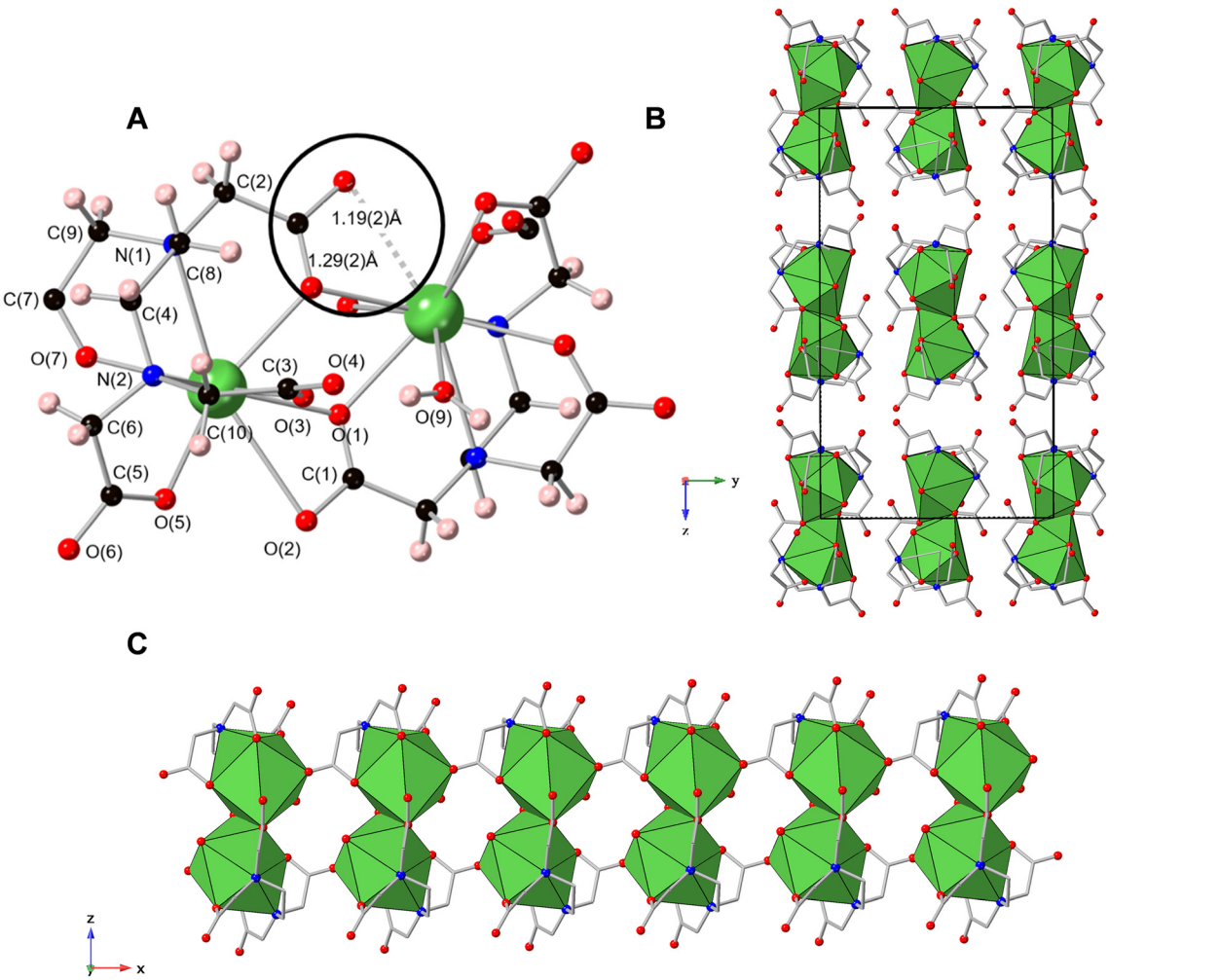

Fig. 2 (A) The coordination environment of **LaEDTA1** represented by a ball-and-stick model. Atom labels are included and the black circle highlights the site of the EDTA protonation. La, O, N, C, and H atoms appear as green, red, blue, black, and pink spheres, respectively. The extended lattice for **LaEDTA1** viewed along the (B) *z*- and (C) *x*-axes highlighting the formation of a 1-D chain from the dimeric La(III) SBUs. La atoms are depicted as green polyhedra, while N and O atoms are shown as blue and red spheres, respectively. H atoms have been omitted for clarity from parts (B) and (C) in the figure.

 This journal is © The Royal Society of Chemistry 2026

Open Access Article. Published on 24 November 2025. Downloaded on 2/15/2026 9:04:38 AM. This article is licensed under a Creative Commons Attribution 3.0 Unported Licence.

which aligns with expectations for μ_2-carboxylate interactions. The longest La–O interaction (La1–O2^2: 2.91(2) Å) falls outside of the typical distance for La–O bonds (2.36–2.74 Å),[68,90,91] suggesting the formation of a weak electrostatic interaction. This is also the site where the structural data suggests protonation of the carboxylate group as C1 shows significant asymmetry, with the C1–O1 bond distance at 1.19(2) Å and the C1–O2 bond distance at 1.29(2) Å. This clear difference is consistent with a localized C=O and C–OH pair, indicative of a protonated carboxylic acid (–COOH). The La–N coordination distances in **LaEDTA1** (La1–N1: 2.81(2) Å, La1–N2: 2.82(2) Å) are longer than the La–O bonds. This trend reflects the preference of La(III) for oxygen donors over nitrogen, due to the greater electronegativity and smaller atomic radius of oxygen. Overall, La–O and La–N bond distances and angles (O4^1–La1–N1 (129.4(4)°) and O7–La1–O1^2 (151.5(5)°)) are consistent with expectations for lanthanide coordination complexes featuring APC ligands, and in agreement with the **LaEDTA1** structure that was obtained previously by Xiong *et al.*[59]

LaEDTA1 contains dimeric secondary building units (SBUs), where La(III) centers are linked *via* μ_2-carboxylate bridging oxygens (Fig. 2B) to form a 1D polymeric chain-like structure linking two La(III) centers per carboxylate oxygen. (Fig. 2C), demonstrating that mechanochemical synthesis can generate hybrid materials as extended networks in REE-APC systems. Beyond the primary μ_2-carboxylate linkages, hydrogen bonding also contributes to the supramolecular assembly of the 1D polymeric chains. Each La(III) center coordinates a single aqua ligand (O9), which acts as a hydrogen-bond donor to a carboxylate oxygen atom (O3) with a donor–acceptor distance of 2.674 Å, indicative of a strong O–H···O interaction. Additional O···O contacts involving the aqua oxygen, such as O9···O1 at 2.938 Å and O9···O7 at 3.162 Å, provide additional connectivity and contribute to dense lattice packing. The restriction to a single coordinated water molecule per La(III), rather than the three to four typically observed in molecular La(III)–EDTA complexes, represents a notable deviation from the expected hydration environment.[68] This reduced water content minimizes void space and solvent-accessible channels, resulting in a more tightly packed lattice.

In addition, Xiong *et al.* used La_2O_3 as a starting material, but their synthetic methodology required the addition of concentrated hydrochloric acid to the initial reaction to generate a lanthanum chloride precursor ahead of the hydrothermal reaction. This also highlights the ability of mechanochemical synthesis to reduce the amount of solvent and eliminate the need to include concentrated acids in synthetic procedures, thereby leading to higher atom efficiency and promoting sustainable material synthesis. Most importantly, mechanochemistry enabled the reaction of an oxide precursor without dissolution and in a much shorter time (five days *vs.* thirty minutes), demonstrating not only a greener approach but also a fundamental difference in reagent reactivity.

Turning our attention to **LaEDTA2**, ED analysis indicates that the compound contains an eight-coordinate cationic La(III) metal center bound to one chloride ligand, three aqua ligands, and four carboxylate oxygens from EDTA, with an overall coordination geometry that is best described as distorted bicapped trigonal prismatic (Fig. 3A). The La–O bond distances (Table S4, SI) range from 2.470(19) to 2.61(2) Å, which are slightly longer than those in **LaEDTA1** (2.43–2.616 Å). The O1, O2, and O3 atoms are assigned as the aqua ligands with bond distances of 2.60(2), 2.61(2), and 2.547(19) Å, respectively. In contrast to **LaEDTA1**, where one carboxylate group remains protonated, the structure of **LaEDTA2** reveals all four carboxylate oxygen atoms from EDTA are bound to the La(III) metal center. This coordination is supported by consistent symmetric or near-symmetric C–O bond distances (C4–O6: 1.26(2) Å and C4–O7: 1.29(2) Å, C1–O4: 1.32(2) Å and C1–O5: 1.280(19) Å) that are characteristic of deprotonated, delocalized –COO$^-$ groups. Whereas none of the C–O bond pairs in **LaEDTA2** exhibits the strong asymmetry characteristic of a protonated –COOH group seen in **LaEDTA1**, the slight elongation of the C4–O7 bond may provide an additional clue to the location of an additional H-atom, which is critical for overall charge neutrality within the compound. Bond length analysis of the amine region reveals that the N1–C00D bond is significantly elongated (1.549(19) Å) and the N1–C3 bond is observed at 1.47(2) Å, consistent with a protonated secondary amine (–NH$_2^+$). Looking closely at the N1 position, we note that it is pointing towards the O7 atom at an interatomic distance of 3.06 Å. This value is within the known range for NH···O donor to acceptor distances that have been reported between 2.6 to 3.2 Å.[92–94] While the structural characterization of **LaEDTA2** suggests that there is disruption of the bonding at the O7 and N1 sites, it is not clear from ED analysis if the hydrogen atom is more strongly associated with the carboxylate or the amine moiety. However, a weak residual density peak (0.27 e$^-$ Å^{-3}) is occasionally observed adjacent to the coordinated nitrogen (N1), suggesting the presence of a disordered N–H atom. Its intermittent appearance across merged data sets indicates partial or dynamic occupancy, which would account for its weak manifestation in the structural model. This interpretation is further corroborated by the fitted IR spectra (Fig. S20–S23, SI), which suggest protonation at the nitrogen site. Secondary amines tend to be protonated at pH values where the solution is acidic, typically below their pK_a values, which in this case are 6.16 and 10.24.[95] However, pK_a values may not be the best predictor herein as they are specifically associated with the tendency of an acid to lose a proton in a solution, which does not fully encompass speciation within the liquid assisted grinding regime that occurs in mechanochemical reactions. Given the donor to acceptor distance between the carboxylate oxygen atom and the central amine, it is possible that hydrogen is disordered between the two groups and is best described as a tautomeric form of the two configurations. Therefore, the hydrogen atom either exists somewhere between these two species or it is disordered throughout the extended lattice. Notably, **LaEDTA2** lacks the La–N coordination observed in **LaEDTA1**,

Open Access Article. Published on 24 November 2025. Downloaded on 2/15/2026 9:04:38 AM.
This article is licensed under a Creative Commons Attribution 3.0 Unported Licence.

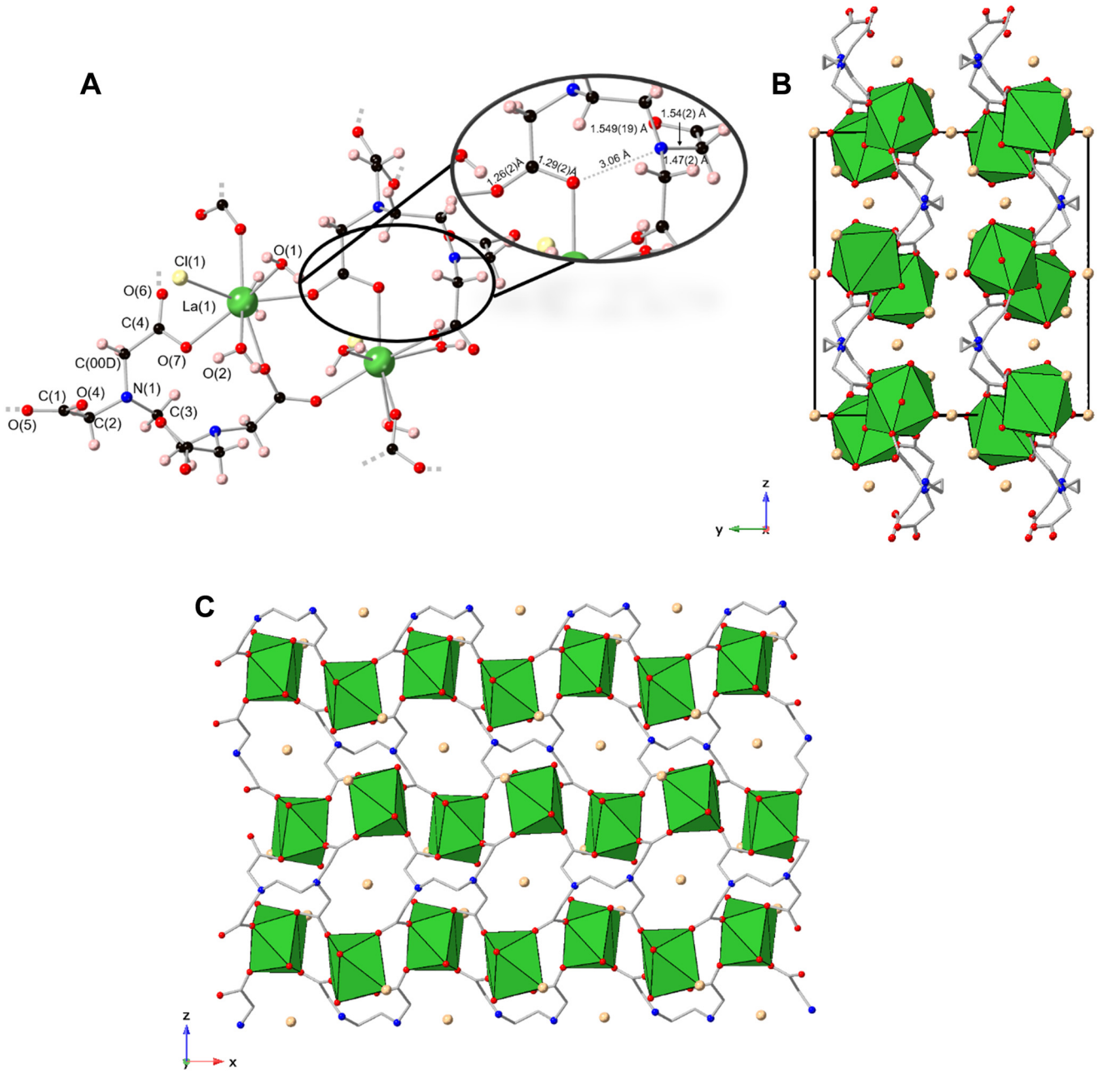

Fig. 3 (A) Ball and stick model highlighting the coordination environment of **LaEDTA2**. La, Cl, O, N, C, and H atoms are depicted as green, yellow, red, blue, black, and pink spheres, respectively. Chlorides in the second coordination sphere were omitted for clarity. (B) Extended lattice for **LaEDTA2** viewed down *z*-axis with H atoms omitted for clarity. La atoms are depicted as green polyhedra while N, O, and Cl atoms are depicted as blue, red, and yellow spheres, respectively. (C) Extended lattice for **LaEDTA2** viewed in the (010) plane where H atoms have been omitted for clarity.

suggesting that the presence of a proton in this region may prevent chelation of the La(III) metal cation, thereby allowing for different assembly motifs to be realized.

In **LaEDTA2**, the EDTA ligand coordinates solely through its four carboxylate oxygens with no nitrogen atoms of the EDTA bonding, leading to different connectivity compared to **LaEDTA1**, and an overall 2D extended network (Fig. 3B and C). Whereas **LaEDTA1** employs μ_2-carboxylate linkages to connect La(III) centers into linear 1D chains, the carboxylate groups in **LaEDTA2** bridge La(III) nodes along *x*- and *z*-directions, generating an extended 2D sheet-like network. The difference in dimensionality arises from the increased angular flexibility afforded by incomplete EDTA coordination, which allows the carboxylates to adopt orientations supporting bidirectional connectivity. Beyond EDTA coordination, the first coordination sphere of **LaEDTA2** contains chloride ions and multiple coordinated water molecules, in contrast to **LaEDTA1**, which results in a change in molecular geometry, and distortion from

 This journal is © The Royal Society of Chemistry 2026

Open Access Article. Published on 24 November 2025. Downloaded on 2/15/2026 9:04:38 AM. This article is licensed under a Creative Commons Attribution 3.0 Unported Licence.

an ideal bicapped trigonal prismatic geometry in **LaEDTA2** is evident in the bond angles O6^{1}–La1–Cl1 (150.5(5)°) and O4–La1–O5^{3} (153.1(5)°). These values are indicative of significant opening of coordination sites to accommodate chloride, and conversely, small angles such as O4–La1–O2 (64.5(6)°) and O3–La1–O5^{3} (68.4(5)°) reflect localized bending. Torsion angles further reveal substantial deviations from planarity within the EDTA ligand as exemplified by O4–C1–C2–N1 (−28.1(18)°) and C3–N1–C2–C1 (156.5(12)°), which highlight bending at the nitrogen–carbon backbones. In addition, torsion angles such as N1–C00D–C4–O6 at 171.9(17)° and N1–C00D–C4–O7 at −9(2)° provide evidence of significant deviations from planar carboxylate coordination. Other larger twists such as C00D–N1–C2–C1 (−76.9(16)°) and C3–N1–C00D–C4 (−66.4(19)°) further demonstrate rotation of carboxylates relative to the ligand backbone. Together, these angular distortions break planarity in multiple directions, straining the EDTA chelator and enabling the more open 2D framework observed for **LaEDTA2**. Moreover, the La–Cl bond distance (La1–Cl1: 2.930(15) Å) falls within the expected range for La–Cl interactions, though it is slightly longer than the typical 2.6–2.9 Å bond distance observed in $LnCl_6^{2-}$ octahedral complexes.[96,97] This elongated La–Cl bond suggests a weaker interaction, which indicates that chloride remains in the first coordination sphere due to limited ligand exchange rather than strong chelation. Additional Cl^- anions are located between the 2-D sheets, which facilitate overall charge neutrality for the structure, and the overall formula for **LaEDTA2** is $[La_2(C_{10}H_{14}N_2O_8)Cl_2(H_2O)_6]Cl_2$.

The 2D sheet-like arrangement of **LaEDTA2** has not been previously reported for solution synthesized La(III)–EDTA systems, as published La(III)–EDTA compounds are either molecular species[87] or 1D polymeric chains.[59] By changing the lanthanum salt precursor in the mechanochemical reaction, chloride ions remain in both the first and second coordination spheres suggesting that this compound may represent a distinct coordination state, where full ligand exchange has not occurred. The use of mechanochemical synthesis allows for access to different ligand binding in La(III)–EDTA compounds, and the existence of **LaEDTA2**, a possible intermediate species, is made possible by stepwise mechanisms that underpin mechanochemical reactions wherein low density, highly solvated products are formed first before subsequent transformation to denser, less solvated materials.[38] This contrasts with solution-based methods that typically yield fully chelated species due to metal–ligand equilibrium driven self-assembly processes.

To confirm that the mechanochemical reactions yielded different results than solution phase reaction, we also performed these experiments with the starting materials (SI, Fig. S29). Solution-phase reactions using La(III) chloride starting material and EDTA yielded only amorphous or unreacted EDTA under ambient conditions (SI, Fig. S30). The La_2O_3 reaction also contained EDTA starting material, but additional features were observed that corresponded to the known $La(H(C_{10}N_2O_8H_{12}))\cdot 7H_2O$ compound,[68] that contains molecular La(III) EDTA complexes with 0-D dimensionality. This data further confirm that crystalline La(III)–EDTA compounds could not be isolated under comparable aqueous conditions.

Bulk materials properties of LaEDTA1 and LaEDTA2. The PXRD patterns from La_2O_3–EDTA and $LaCl_3\cdot 7H_2O$–EDTA reactions were compared to the structures obtained from ED analysis to confirm bulk purity of the samples. The simulated pattern for **LaEDTA1** agrees well with the product formed from the La_2O_3–EDTA mechanochemical reaction, with no distinct observable impurities from the starting materials (Fig. S7, SI). The PXRD pattern of the $LaCl_3\cdot 7H_2O$–EDTA reaction product is mostly in agreement with the simulated pattern for **LaEDTA2**; however, we do note some slight differences between experimental and simulated patterns that are suggestive of minor heterogeneities within the sample (Fig. S8, SI). The longer-term stabilities of **LaEDTA1** and **LaEDTA2** were also monitored to further understand the overall bulk properties of the materials with PXRD patterns collected on days 0, 3, 5, and 7 (Fig. S9 and S10, SI). Though there is a slight decrease in intensities over time, consistent peak positions across all time points indicate that the crystallinity of both phases are maintained, confirming the structural integrity of the La(III)–EDTA compounds formed from mechanochemical reactions.

The purity of mechanochemical bulk products was also probed using field-emission scanning electron microscopy coupled with energy-dispersive X-ray spectroscopy (FE-SEM/EDS). These techniques are widely used in materials chemistry to evaluate surface morphology and elemental composition, particularly when assessing the homogeneity and potential contamination of the synthesized products as EDS mapping enables semi-quantitative detection of elemental species distributed across sample surfaces. In the case of **LaEDTA1**, the sample was carbon-coated for analysis and elemental mapping revealed a uniform distribution of La, O, N, and C throughout the entire sample (Fig. 4 and S25, SI). For **LaEDTA2**, which was gold-coated due to charging issues, Cl was also detected in addition to La, O, N, and C (Fig. 5 and S26, SI). Both of these results are consistent with expectations as these elements constitute the primary components of La–EDTA coordination networks based on ED structural analysis. Additionally, trace signals of Fe were also observed in both samples, which likely originated from the stainless-steel milling media. This suggests that the ball milling media may have been partially incorporated into the final product, as shown in elemental mapping *via* FE-SEM/EDS analysis (Fig. 4 and 5). Notably, this factor is less prominent in **LaEDTA2** compared to **LaEDTA1**, since its starting material, $LaCl_3\cdot 7H_2O$, is softer than La_2O_3. Due to the lower hardness of lanthanum chloride compared to lanthanum oxide,[83] it is less likely to shear off metals from the stainless-steel milling media (*e.g.*, Fe(III)), thus reducing the risk of inadvertent complexation or contamination. These results emphasize the importance of considering precursor hardness and mechanical abrasion, especially in mechanochemical reactions, as they can directly influence

Open Access Article. Published on 24 November 2025. Downloaded on 2/15/2026 9:04:38 AM. This article is licensed under a Creative Commons Attribution 3.0 Unported Licence.

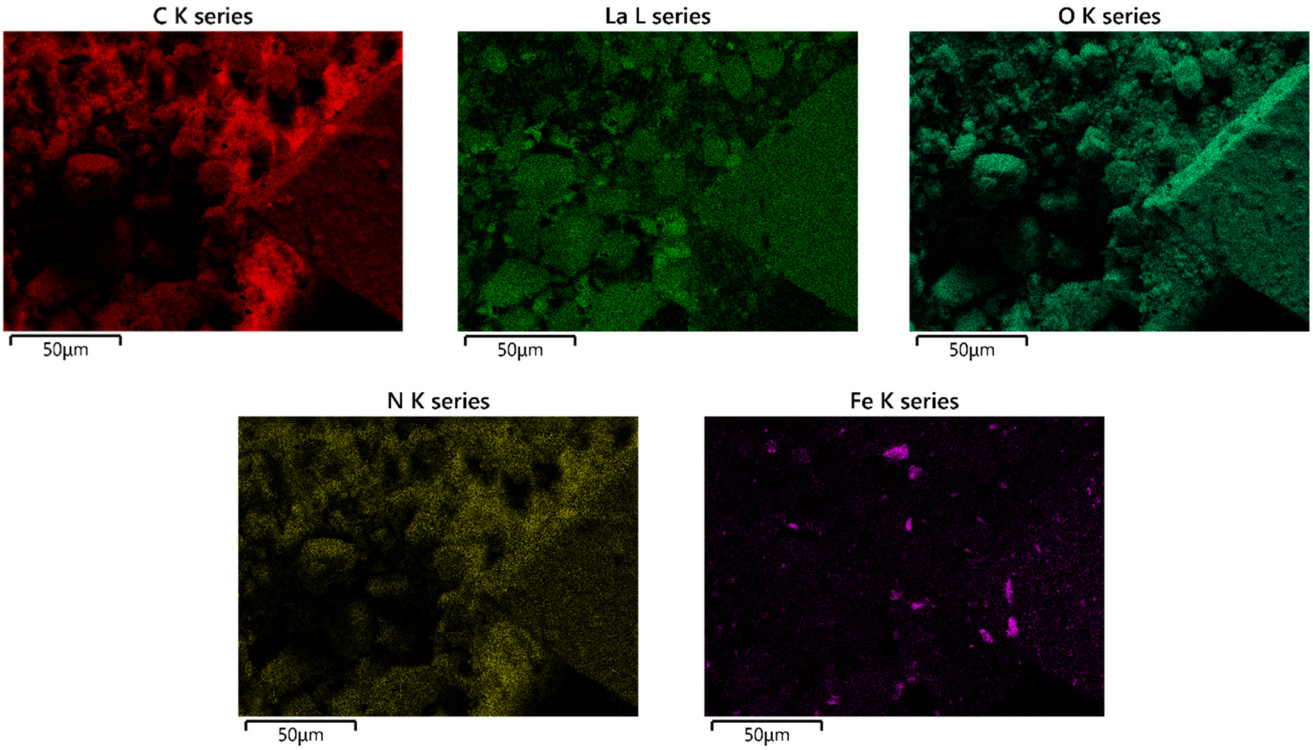

Fig. 4 Elemental mapping analysis of **LaEDTA1** obtained from FE-SEM-EDS measurements. Sample material was carbon-coated to prevent surface charging and to improve image quality.

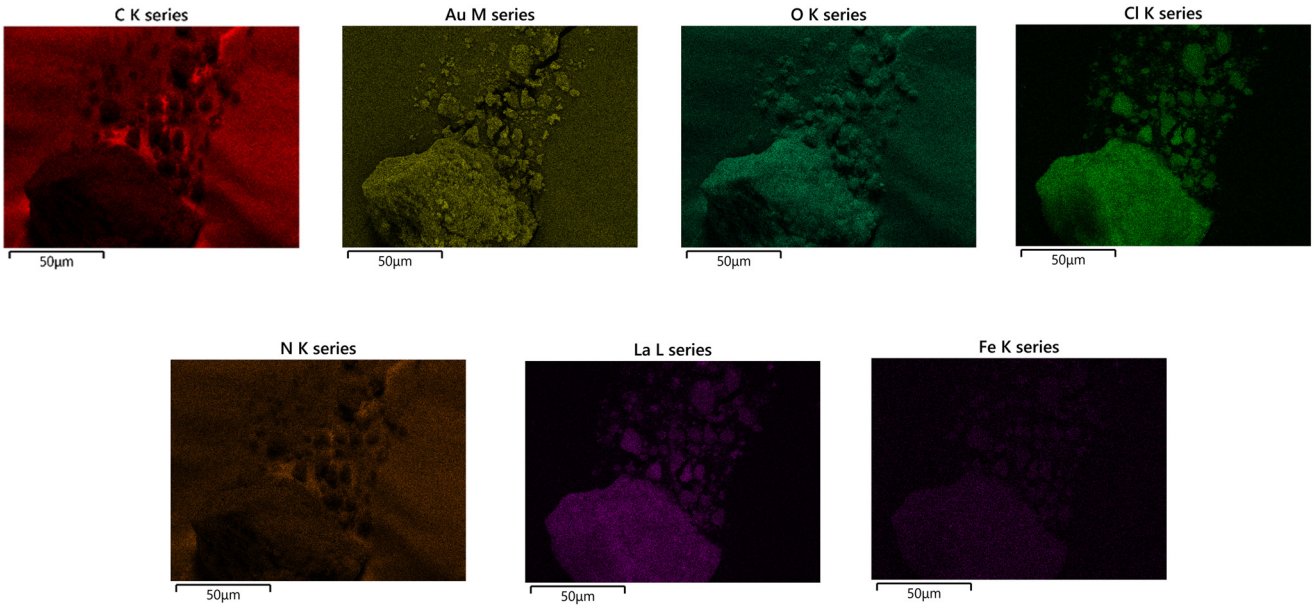

Fig. 5 Elemental mapping analysis of **LaEDTA2** obtained by FE-SEM-EDS. Material was gold-coated to prevent surface charging during analysis.

the compositional purity of the final product. In addition, mechanochemical milling time also appears to influence sample purity and contamination. Štefanić *et al.* demonstrated that prolonged high-energy milling increases contamination risks from stainless-steel components due to progressive abrasion of the milling tools, leading to a threefold increase in impurities in longer reactions.[98] In our system, **LaEDTA2** is milled for only fifteen minutes and displays noticeably lower contamination compared to the thirty-minute reaction used to prepare **LaEDTA1**, suggesting that shorter milling durations might also play a role in minimizing Fe contamination.

 This journal is © The Royal Society of Chemistry 2026

Open Access Article. Published on 24 November 2025. Downloaded on 2/15/2026 9:04:38 AM. This article is licensed under a Creative Commons Attribution 3.0 Unported Licence.

Vibrational spectroscopic analysis of **LaEDTA1** confirms the metal coordination features observed in the solid-state compound *via* ED. The IR spectrum of **LaEDTA1** was closely analyzed by fitting the spectral windows between 3600–2800 and 1800–1000 cm^{-1} (Fig. S18 and S19, SI). In the IR spectrum of **LaEDTA1** (Fig. 6), there is a shoulder peak at 1694 cm^{-1} that is consistent with a single C=O stretching mode, which we attribute to one protonated carboxylic acid group (–COOH). Moreover, a strong band observed at 1584 cm^{-1} corresponds to an asymmetric carboxylate (COO^-) group stretching vibration, while the symmetric stretching mode appears at 1415 cm^{-1}, which confirms the presence of three deprotonated carboxylate groups (COO^-) coordinated to the La(III) center. The difference between these two vibrational modes ($\Delta\nu$ = 169 cm^{-1}) suggests a chelating or bridging coordination mode, and this finding is consistent with the ED structure for **LaEDTA1**. The broad band centered around 1666 cm^{-1} is attributed to the deformation mode of coordinated water molecules, further supporting the hydrated nature of the compound. Peaks observed in the 2986–2845 cm^{-1} region correspond to C–H stretching vibrations of the ethylene backbone of EDTA, and broad bands at 3505, 3372, and 3227 cm^{-1} are assigned to O–H stretching vibrations from –COOH groups as well as coordinated lattice water molecules. Typically, IR spectra of metal oxides, including lanthanum oxide, have bands in the region of 800–400 cm^{-1}, corresponding to metal–oxygen (M–O) stretching frequencies, and in the spectrum of **LaEDTA1** peaks at 823 and 449 cm^{-1} can be attributed to La–O stretching vibrations, consistent with previously reported La–O stretches at 854 and 467 cm^{-1} in lanthanum oxide.[99] Furthermore, a weak band at 643 cm^{-1} may be attributed to a La–OH stretching mode, as it matches with previous reports for La(III) hydroxide species, and this provides additional evidence that the residual oxide starting material forms some amount of La(III) hydroxide in the LAG-mediated reaction.[100]

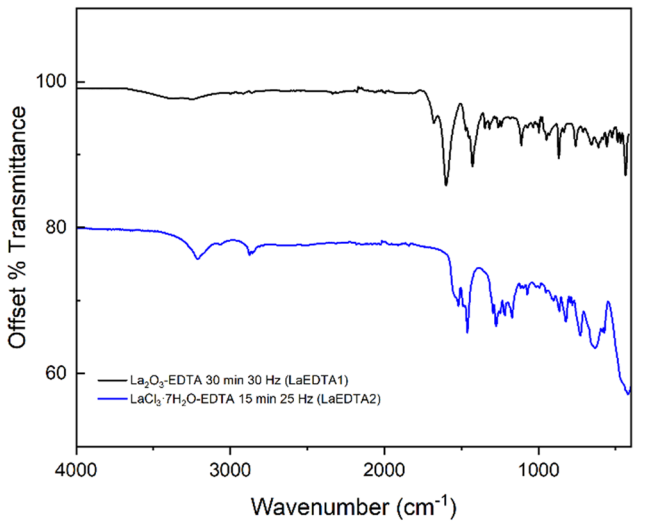

Fig. 6 Mid-IR spectra of **LaEDTA1** (top) and **LaEDTA2** (bottom) collected in the 4000–400 cm^{-1} spectral window.

In contrast, the IR spectrum of **LaEDTA2** (Fig. 6) exhibits notable differences in vibrational modes, reflecting its distinct coordination environment. The IR spectrum of **LaEDTA2** was closely analyzed by fitting the spectral windows between 3500–3100, 3100–2900, 1800–1300, and 1300–950 cm^{-1} (Fig. S20–S23, SI). The asymmetric and symmetric carboxylate ($-COO^-$) stretching vibrations appear at 1607 and 1417 cm^{-1}, respectively, yielding a $\Delta\nu$ value of 190 cm^{-1}. This shift, larger than that observed in **LaEDTA1**, suggests a different carboxylate binding mode, most likely influenced by the presence of chloride ions in the first coordination sphere, indicating a greater contribution from monodentate or asymmetric binding modes rather than the more uniform bridging coordination observed in **LaEDTA1**. Additionally, a broad O–H stretching band appears at 3491, 3458, and 3410 cm^{-1} confirming the presence of coordinated water molecules, which is further supported by bending vibrations in the 1686–1660 cm^{-1} range. These features align with the electron diffraction derived crystal structure for **LaEDTA2**, where La(III) coordinates to three aqua ligands. Overlapping bands at 3266, 3255, and 3203 cm^{-1} as well as bands at 3354 and 3304 cm^{-1} may be attributed to N–H symmetric stretching vibrations of protonated secondary amine groups ($-NH_2^+$), also suggesting that both nitrogen donor atoms are protonated in this system. A distinct band at 1630 cm^{-1} is attributed to N–H bending, while some of the features in the 1450–1250 cm^{-1} region were assigned to N–H wagging modes, again collectively suggest the presence of two protonated amines in the structure. The lower frequency region also provides key evidence for La–O coordination, with peaks at 775, 727, 709, and 455 cm^{-1} aligning with the reported range for La–O stretching vibrations (854–467 cm^{-1}).[99] However, compared to **LaEDTA1**, these slightly lower vibrational frequencies suggest weaker La–O interactions, likely due to the reduced denticity and distorted coordination environment of EDTA in **LaEDTA2**.

Thermal stability and decomposition for both **LaEDTA1** (Fig. 7A) and **LaEDTA2** (Fig. 7B) were investigated using thermogravimetric analysis (TGA) and differential scanning calorimetry (DSC). The TGA profile of **LaEDTA1** shows a total mass loss of ~49%, occurring in multiple distinct steps. The first weight loss of ~4%, occurring between 50–79 °C corresponds to the loss of bound water molecules. This is accompanied by an endothermic peak in the DSC curve, indicating a dehydration process. The second weight loss of ~7%, occurring between 79–247 °C, was likely caused by the initial decomposition of the EDTA ligand, followed by a third weight loss of ~16%, observed between 247–376 °C that can be attributed to further decomposition of the EDTA ligand. These two steps yield small endothermic peaks in the related DSC curve. The most significant decomposition event occurs in the range of 376–464 °C, accounting for ~17% mass loss, which corresponds to the breakdown of the organic backbone of EDTA. This step is marked by a pronounced endothermic transition, suggesting metal–ligand bond cleavage and

Open Access Article. Published on 24 November 2025. Downloaded on 2/15/2026 9:04:38 AM.
This article is licensed under a Creative Commons Attribution 3.0 Unported Licence.

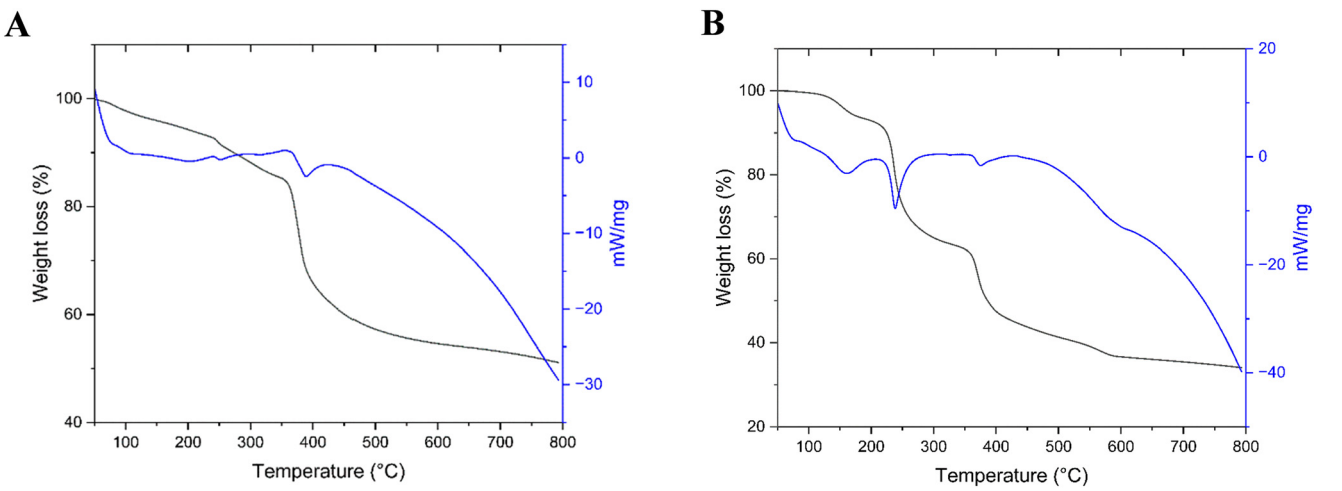

Fig. 7 TGA-DSC graph of (A) **LaEDTA1** and (B) **LaEDTA2** where TGA curves are shown in black and DSC curves are shown in blue.

structural collapse of the coordination framework. These results align with literature reports and our experimental TGA data for EDTA itself (Fig. S24, SI), where the ligand remains stable until 200–250 °C, after which significant decomposition occurs between 250–320 °C. A final weight loss of ~5% occurs between 464–700 °C, attributed to combustion of residual organic fragments. Beyond 700 °C, the decomposition is complete, and the curve starts to plateau, with a remaining mass of 51% that reflects partial conversion to hexagonal La_2O_3 as well as additional minor phases that could not be identified *via* PXRD analysis (Fig. S11, SI).

Compared to **LaEDTA1**, the thermal decomposition of **LaEDTA2** follows a more stepwise pathway, most likely due to the presence of chloride ions and additional coordinated water molecules in its structure, and the TGA profile for **LaEDTA2** reveals a total mass loss of approximately 65% that occurs over multiple steps. The first decomposition events occur between 50–78 °C and 78–149 °C, corresponding to a total ~4% weight loss, which can be attributed to the release of water molecules. This dehydration step is marked by an endothermic peak in the DSC curve, indicating sufficient energy has been added to disrupt hydrogen bonding and remove water from the coordination sphere. A second weight loss of ~14% occurs in the range of 149–238 °C, which is assigned to the partial decomposition of the EDTA ligand, likely involving cleavage of carboxylate functional groups, and the gradual release of chloride ions. This process is accompanied by a mild endothermic transition, suggesting a stepwise degradation influenced by the presence of anions in the coordination sphere. A significant mass loss of ~27% between 238–371 °C and a mass loss of ~18% between 371–570 °C both correspond to the degradation of the organic backbone of the EDTA ligand. This major decomposition step, characterized by a broad endothermic DSC peak, suggests a gradual breakdown of the coordination network, likely due to the influence of chloride ions stabilizing partial intermediates during thermal decomposition. The final decomposition stage occurs between 570–700 °C, accounting for ~2% mass loss, and is attributed to the complete combustion of remaining organic residues and the removal of volatile chloride species. However, achieving complete combustion of EDTA was challenging for this compound, as evidenced by experimental EA results that did align well with the theoretical calculations for C, H, and N within the material (Tables S11 and S12, SI). Ultimately, beyond 700 °C, no further decomposition occurs, and the remaining mass of 35% could not be identified using PXRD analysis (Fig. S12, SI).

4. Conclusions

This study highlights the versatility of mechanochemical synthesis for generating rare-earth hybrid materials with varying dimensionalities. Through a systematic evaluation of lanthanum salt precursors, milling frequencies, reaction times, and metal-to-ligand ratios, we demonstrated that small changes in synthetic conditions can result in different La(III)–EDTA architectures. Specifically, as exemplified by two representative materials, the use of La_2O_3 under optimized LAG conditions led to a 1D chain structure, while switching to $LaCl_3{\cdot}7H_2O$ as a starting material resulted in a cationic 2D sheet-like structure with chloride anions retained in the outer sphere. These findings emphasize that the nature and reactivity of the starting metal salt strongly influence coordination outcomes, an important consideration for advancing mechanochemistry as a platform for rare-earth materials design. Structural elucidation by MicroED enabled precise insight into both compounds, reinforcing the growing utility of this technique for characterizing hybrid materials when traditional SCXRD is inaccessible. Complementary characterizations using PXRD, FTIR, EA, and TGA confirmed product phase formation, thermal behavior, and composition. FE-SEM/EDS analysis further revealed the homogeneity and purity of the final materials, while also drawing attention to the potential influence of milling media on trace element incorporation. Overall, these results demonstrate that mechanochemistry can be used to expand the accessible chemical space for rare-earth

 This journal is © The Royal Society of Chemistry 2026

Open Access Article. Published on 24 November 2025. Downloaded on 2/15/2026 9:04:38 AM. This article is licensed under a Creative Commons Attribution 3.0 Unported Licence.

aminopolycarboxylates in the solid state *via* efficient, solvent-minimized synthetic approaches within short periods of times under mild conditions.

Conflicts of interest

The authors declare no financial or non-financial competing interests.

Data availability

The data supporting this article have been included as part of the supplementary information (SI).

Supplementary information: the SI is available including synthetic details, crystallographic data and details, electron diffraction datasets and details, PXRD patterns, Whole Pattern Fitting (WPF) reports, IR spectra of all materials, fitted IR spectra with vibrational mode assignments, the TGA curve of EDTA, PXRD of residue analyses, elemental analysis results, and FE-SEM/EDS images for lanthanum–EDTA compounds discussed in the manuscript (PDF).

CCDC 2491564 and 2491565 contain the supplementary crystallographic data for this paper.[101a,b]

Acknowledgements

The work was supported by start-up funding from the College of Liberal Arts and Sciences and the Department of Chemistry at the University of Iowa. We acknowledge the University of Iowa Materials, Analysis, Testing, and Fabrication Facility for use of the powder X-ray diffractometer, thermogravimetric analyzer, elemental analyzer, and scanning electron microscope used in this study. We would specifically like to thank MATFab staff members Dr. Daniel Unruh and Dr. Michael Sinnwell for support associated with PXRD, EA, and FE-SEM/EDS measurements. We also thank Prof. Scott R. Daly for providing access to the ball mill used in our preliminary experiments. Field emission SEM/EDS data were collected on an instrument funded by NSF Award EAR-2215495. Mid-IR spectra were collected on an instrument funded by a Nuclear Regulatory Commission Faculty Development Grant (NRC 31310018M0042).

References

1 H. Furukawa, M. Cordova, M. O'Keeffe and O. Yaghi, *Science*, 2013, **341**, 1230444, DOI: 10.1126/science.1230444.
2 P. Gomez-Romero, A. Pokhriyal, D. Rueda-García, L. N. Bengoa and R. M. González-Gil, *Chem. Mater.*, 2024, **36**(1), 8–27, DOI: 10.1021/acs.chemmater.3c01878.
3 S. Afrin, M. W. Khan, E. Haque, B. Ren and J. Z. Ou, *J. Colloid Interface Sci.*, 2022, **623**, 378–404, DOI: 10.1016/j.jcis.2022.05.026.
4 T. R. Cook, Y. R. Zheng and P. J. Stang, *Chem. Rev.*, 2013, **113**(1), 734–777, DOI: 10.1021/cr3002824.
5 K. O. Kirlikovali, S. L. Hanna, F. A. Son and O. K. Farha, *ACS Nanosci. Au*, 2023, **3**(1), 37–45, DOI: 10.1021/acsnanoscienceau.2c00046.
6 M. L. Tong and X. M. Chen, *Synthesis of Coordination Compounds and Coordination Polymers In Modern Inorganic Synthetic Chemistry*, Elsevier, 2nd edn, 2017, ch. 8.
7 M. J. McDermott, B. C. McBride, C. E. Regier, G. T. Tran, Y. Chen, A. A. Corrao, M. C. Gallant, G. E. Kamm, C. J. Bartel, K. W. Chapman, P. G. Khalifah, G. Ceder, J. R. Neilson and K. A. Persson, *ACS Cent. Sci.*, 2023, **9**(10), 1957–1975, DOI: 10.1021/acscentsci.3c01051.
8 K. J. Ardilo-Fierro and J. G. Hernandez, *ChemSusChem*, 2021, **14**(10), 2145–2162, DOI: 10.1002/cssc.202100478.
9 Z. Chen, G. F. Han, A. Mahmood, J. Hou, W. Wei, S. B. Kyong and B. J. Ni, *Prog. Mater. Sci.*, 2024, **145**, 101299, DOI: 10.1016/j.pmatsci.2024.101299.
10 A. P. Amrute, B. Zibrowius and F. Schüth, *Chem. Mater.*, 2020, **32**(11), 4699–4706, DOI: 10.1021/acs.chemmater.0c01266.
11 A. Aleksandrov, A. Zelenetskii, A. Ivanovich, A. A. Dubinskii, O. G. Garkusha, A. I. Prokof'ev and N. N. Bubnov, *Dokl. Phys. Chem.*, 2000, **375**, 215–217.
12 A. B. Chetry, *J. Chem. Res.*, 2025, **49**(3), DOI: 10.1177/17475198251339299.
13 S. Darwish, S. Q. Wang, D. M. Croker, G. M. Walker and M. J. Zaworotko, *ACS Sustainable Chem. Eng.*, 2019, **7**(24), 19505–19512, DOI: 10.1021/acssuschemeng.9b04552.
14 S. L. James, C. J. Adams, C. Bolm, D. Braga, P. Collier, T. Friščić, F. Grepioni, K. D. M. Harris, G. Hyett, W. Jones, A. Krebs, J. Meck, L. Maini, A. G. Orpen, I. P. Parkin, W. C. Shearouse, J. W. Steed and D. C. Waddell, *Chem. Soc. Rev.*, 2012, **41**(1), 413–447, DOI: 10.1039/C1CS15171A.
15 S. Głowniak, B. Szczęśniak, J. Choma and M. Jaroniec, *Mater. Today*, 2021, **46**, 109–124, DOI: 10.1016/j.mattod.2021.01.008.
16 P. Baláž, M. Achimovičová, M. Baláž, P. Billik, Z. Cherkezova-Zheleva, J. M. Criado, F. Delogu, E. Dutková, E. Gaffet, F. J. Gotor, R. Kumar, I. Mitov, T. Rodaj, M. Senna, A. Streletskii and K. Wieczorek-Ciurowa, *Chem. Soc. Rev.*, 2013, **42**(18), 7571–7637, DOI: 10.1039/C3CS35468G.
17 E. Boldyreva, *Chem. Soc. Rev.*, 2013, **42**(18), 7719–7738, DOI: 10.1039/C3CS60052A.
18 T. Friščić, *J. Mater. Chem.*, 2010, **20**(36), 7599–7605, DOI: 10.1039/C0JM00872A.
19 B. S. Pladevall, A. de Aguirre and F. Maseras, *ChemSusChem*, 2021, **14**(13), 2763–2768, DOI: 10.1002/cssc.202100497.
20 T. Friščić and L. Fábián, *CrystEngComm*, 2009, **11**(5), 743–745, DOI: 10.1039/B822934C.
21 R. J. Allenbaugh and A. Shaw, *Results Chem.*, 2023, **5**, 100827, DOI: 10.1016/j.rechem.2023.100827.
22 J. Huot, F. Cuevas, S. Deledda, K. Edalati, Y. Filinchuk, T. Grosdidier, B. C. Hauback, M. Heere, T. R. Jensen, M. Latroche and S. Sartori, *Materials*, 2019, **12**(17), 2778, DOI: 10.3390/ma12172778.
23 Q. Tan and J. Li, *Environ. Sci. Technol.*, 2015, **49**(10), 5849–5861, DOI: 10.1021/es506016w.
24 P. Ying, J. Yu and W. Su, *Adv. Synth. Catal.*, 2021, **363**(5), 1246–1271, DOI: 10.1002/adsc.202001245.

Open Access Article. Published on 24 November 2025. Downloaded on 2/15/2026 9:04:38 AM. This article is licensed under a Creative Commons Attribution 3.0 Unported Licence.

25 L. E. Wenger and T. P. Hanusa, *Chem. Commun.*, 2023, **59**(96), 14210–14222, DOI: 10.1039/D3CC04929A.
26 S. Mateti, M. Mathesh, Z. Liu, T. Tao, T. Ramireddy, A. M. Glushenkov, W. Yang and Y. I. Chen, *Chem. Commun.*, 2021, **57**(9), 1080–1092, DOI: 10.1039/D0CC06581A.
27 P. Zhang and S. Dai, *J. Mater. Chem. A*, 2017, **5**(31), 16118–16127, DOI: 10.1039/C7TA04829G.
28 G. W. Wang, *Chem. Soc. Rev.*, 2013, **42**(18), 7668–7700, DOI: 10.1039/C3CS35526H.
29 V. Štrukil, *Synlett*, 2018, **29**, 1281–1288, DOI: 10.1055/s-0036-1591868.
30 D. Tan and T. Friscic, *Eur. J. Org. Chem.*, 2017, **2018**, 18–33, DOI: 10.1002/ejoc.201700961.
31 N. R. Rightmire and T. P. Hanusa, *Dalton Trans.*, 2016, **45**(6), 2352–2362, DOI: 10.1039/C5DT03866A.
32 A. L. Garay, A. Pichon and S. L. James, *Chem. Soc. Rev.*, 2007, **36**(6), 846–855, DOI: 10.1039/B600363J.
33 A. Beillard, X. Bantreil, T. X. Métro, J. Martinez and F. Lamaty, *Chem. Rev.*, 2019, **119**(12), 7529–7609, DOI: 10.1021/acs.chemrev.8b00479.
34 T. V. Fetrow and S. R. Daly, *Dalton Trans.*, 2021, **50**(33), 11472–11484, DOI: 10.1039/D1DT01932E.
35 D. V. Kravchuk and T. Z. Forbes, *CrystEngComm*, 2022, **24**(4), 775–781, DOI: 10.1039/D1CE01479J.
36 D. V. Kravchuk and T. Z. Forbes, *Chem. Commun.*, 2022, **58**(28), 4528–4531, DOI: 10.1039/D2CC00242F.
37 W. Jones and M. D. Eddleston, *Faraday Discuss.*, 2014, **170**, 9–34, DOI: 10.1039/C4FD00162A.
38 J. L. Do and T. Friščić, *ACS Cent. Sci.*, 2017, **3**(1), 13–19, DOI: 10.1021/acscentsci.6b00277.
39 F. Cuccu, L. De Luca, F. Delogu, E. Colacino, N. Solin, R. Mocci and A. Porcheddu, *ChemSusChem*, 2022, **15**(17), e202200362, DOI: 10.1002/cssc.202200362.
40 A. Bragrsen, L. Maini, M. Curzi and M. Polito, *Dalton Trans.*, 2006, 1249–1263, DOI: 10.1039/B516165G.
41 F. Lorenzo, C. Katsavou, K. Parada Rolán, S. Dias, H. Fernández Cortés, J. Collado, F. J. Chichón, R. Arranz, C. Santiago and E. C. Sañudo, *Inorg. Chem.*, 2025, **64**(27), 13824–13829, DOI: 10.1021/acs.inorgchem.5c01592.
42 S. Cotton, Coordination Chemistry of the Lanthanides, in *Lanthanide and Actinide Chemistry*, 2006, pp. 35–60.
43 T. Moeller, D. F. Martin, L. C. Thompson, R. Ferrús, G. R. Feistel and W. J. Randall, *Chem. Rev.*, 1965, **65**(1), 1–50, DOI: 10.1021/cr60233a001.
44 R. M. Smith and A. E. Martell, *Sci. Total Environ.*, 1987, **64**(1), 125–147, DOI: 10.1016/0048-9697(87)90127-6.
45 P. K. Tse and J. E. Powell, *Inorg. Chem.*, 1985, **24**(18), 2727–2730, DOI: 10.1021/ic00212a005.
46 K. L. Nash, *Solvent Extr. Ion Exch.*, 2015, **33**(1), 1–55, DOI: 10.1080/07366299.2014.985912.
47 T. S. Grimes, R. C. Heathman, S. Jansone-Popova, V. S. Bryantsev, S. Goverapet Srinivasan, M. Nakase and P. R. Zalupski, *Inorg. Chem.*, 2017, **56**(3), 1722–1733, DOI: 10.1021/acs.inorgchem.6b02897.
48 P. R. Zalupski, T. S. Grimes, C. D. Pilgrim, C. R. Heathman, S. Jansone-Popova, K. R. Johnson, V. Bryantsev and R. C. Chapleski, Aminopolycarboxylates in trivalent f-element separations, in *Handbook on the Physics and Chemistry of Rare Earths*, Elsevier, 2021, ch. 320, vol. 60, pp. 1–162.
49 J. R. Hart, Ethylenediaminetetraacetic Acid and Related Chelating Agents, in *Ullmann's Encyclopedia of Industrial Chemistry*, 2011.
50 A. S. A. Al Sheidi, *Crystals*, 2024, **14**(10), 829.
51 Y. El Ouardi, S. Virolainen, E. Salomon Massima Mouele, M. Laatikainen, E. Repo and K. Laatikainen, *Hydrometallurgy*, 2023, **218**, 106047, DOI: 10.1016/j.hydromet.2023.106047.
52 G. C. Silva, C. Souza, P. A. Ferreira, P. L. Nazareth and A. C. Ladeira, *Minerals*, 2024, **14**(5), 451, DOI: 10.3390/min14050451.
53 H. Hasegawa, A. Z. Begum, R. Murase, K. Ishii, H. Sawai, A. S. Mashio, T. Maki and I. M. M. Rahman, *Waste Manage.*, 2018, **80**, 17–25.
54 M. Xing, X. Wu, Z. Li, F. Zhang, Y. Wang and L. Zhao, *Process Saf. Environ. Prot.*, 2023, **175**, 60–69, DOI: 10.1016/j.psep.2023.05.022.
55 J. C. Belmont-Sánchez, N. Ruiz-González, A. Frontera, A. Matilla-Hernández, A. Castiñeiras and J. Niclós-Gutiérrez, *Crystals*, 2020, **10**(4), 304, DOI: 10.3390/cryst10040304.
56 R. Mudsainiyan, *J. Solid State Chem.*, 2015, **230**, 61–69, DOI: 10.1016/j.jssc.2015.04.001.
57 S. Durand, J. P. Dognon, P. Guilbaud, C. Rabbe and G. Wipff, *J. Chem. Soc., Perkin Trans. 2*, 2000, **4**, 705–714, DOI: 10.1039/A908879B.
58 K. Furukawa, Y. Takahashi and H. Sato, *Geochim. Cosmochim. Acta*, 2007, **71**(18), 4416–4424, DOI: 10.1016/j.gca.2007.07.009.
59 D. B. Xiong, H. H. Chen and X. X. Yang, *Inorg. Chim. Acta*, 2007, **360**(5), 1616–1620, DOI: 10.1016/j.ica.2006.08.044.
60 R. Baggio and M. Perec, *Inorg. Chem.*, 2004, **43**(22), 6965–6968, DOI: 10.1021/ic049165p.
61 M. F. P. da Silva, J. R. Matos and P. C. Isolani, *J. Therm. Anal. Calorim.*, 2008, **94**(1), 305–311, DOI: 10.1007/s10973-007-8906-x.
62 V. Kiritsis, A. Michaelides, S. Skoulika, S. Golhen and L. Ouahab, *Inorg. Chem.*, 1998, **37**(13), 3407–3410, DOI: 10.1021/ic980014u.
63 A. Smerigan, S. Biswas, F. D. Vila, J. Hong, R. B. Per Getman and S. R. Bare, *Inorg. Chem.*, 2023, **62**(36), 14523–14532, DOI: 10.1021/acs.inorgchem.3c01334.
64 N. Sakagami, Y. Yamada, T. Konno and K. I. Okamoto, *Inorg. Chim. Acta*, 1999, **288**(1), 7–16, DOI: 10.1016/S0020-1693(99)00005-5.
65 D. L. Long, A. J. Blake, N. R. Champness, C. Wilson and M. Schröder, *Angew. Chem., Int. Ed.*, 2001, **40**(13), 2443–2447, DOI: 10.1002/1521-3773(20010702)40.
66 J. A. Mattocks and J. A. Cotruvo, *Chem. Soc. Rev.*, 2020, **49**(22), 8315–8334, DOI: 10.1039/D0CS00653J.
67 S. P. Fricker, *Chem. Soc. Rev.*, 2006, **35**(6), 524–533, DOI: 10.1039/B509608C.
68 M. D. Lind, B. Lee and J. L. Hoard, *J. Am. Chem. Soc.*, 1965, **87**(7), 1611–1612, DOI: 10.1021/ja01085a036.
69 F. Xie, T. A. Zhang, D. Dreisinger and F. Doyle, *Miner. Eng.*, 2014, **56**, 10–28, DOI: 10.1016/j.mineng.2013.10.021.
70 X. Zhou, E. I. Vovk, Y. Liu, C. Guan and Y. Yang, *Front. Chem.*, 2021, **9**, 694559, DOI: 10.3389/fchem.2021.694559.

 This journal is © The Royal Society of Chemistry 2026

Open Access Article. Published on 24 November 2025. Downloaded on 2/15/2026 9:04:38 AM. This article is licensed under a Creative Commons Attribution 3.0 Unported Licence.

71 M. P. Snelgrove, B. Doñagueda Suso, C. S. Sangster, K. Asif, E. Regincós Martí, D. J. Ashworth, J. P. Tidey, J. R. B. Gomes, M. Jorge, A. R. Kennedy, S. Parsons, A. Fletcher and G. A. Craig, *Angew. Chem., Int. Ed.*, 2025, **64**(43), e202514527, DOI: 10.1002/anie.202514527.
72 J. R. Blanton, R. J. Papoular and D. Louër, *Powder Diffr.*, 2019, **34**(3), 233–241, DOI: 10.1017/S0885715619000514.
73 *CrystalMaker*, CrystalMaker Software Ltd, Begbroke, Oxfordshire, England, 2014.
74 *JADE*, Materials Data, Livermore, CA, 2019.
75 S. Ito, F. J. White, E. Okunishi, Y. Aoyama, A. Yamano, H. Sato, J. D. Ferrara, M. Jasnowsk and M. Meyer, *CrystEngComm*, 2021, **23**(48), 8622–8630, DOI: 10.1039/D1CE01172C.
76 *CrysAlisPro Software system*, Rigaku Corporation, Wroclaw, Poland, 2023.
77 G. Sheldrick, *Acta Crystallogr., Sect. A: Found. Adv.*, 2015, **71**(1), 3–8, DOI: 10.1107/S2053273314026370.
78 *AutoChem 6.0.5*, Rigaku Corporation, Wroclaw, Poland, 2023.
79 O. V. Dolomanov, L. J. Bourhis, R. J. Gildea, J. A. K. Howard and H. Puschmann, *J. Appl. Crystallogr.*, 2009, **42**(2), 339–341, DOI: 10.1107/S0021889808042726.
80 G. Sheldrick, *Acta Crystallogr., Sect. C: Struct. Chem.*, 2015, **71**(1), 3–8.
81 F. Fischer, *Phys. Chem. Chem. Phys.*, 2016, **18**(33), 23320–23325, DOI: 10.1039/C6CP04280E.
82 T. Friscic, *J. Mater. Chem.*, 2010, **20**, 36, DOI: 10.1039/c0jm00872a.
83 S. H. Mirza, M. Zulfiqar and S. Azam, *Phys. B*, 2024, **676**, 415686, DOI: 10.1016/j.physb.2024.415686.
84 C. J. Adams, M. A. Kurawa, M. Lusi and A. G. Orpen, *CrystEngComm*, 2008, **10**(12), 1790–1795, DOI: 10.1039/B809950B.
85 P. Fleming, R. A. Farrell, J. D. Holmes and M. A. Morris, *J. Am. Ceram. Soc.*, 2010, **93**(4), 1187–1194, DOI: 10.1111/j.1551-2916.2009.03564.x.
86 J. Lee, Q. Zhang and F. Saito, *J. Solid State Chem.*, 2001, **160**(2), 469–473, DOI: 10.1006/jssc.2001.9276.
87 C. F. G. C. Geraldes, A. M. Urbano, M. A. Hoefnagel and J. A. Peters, *Inorg. Chem.*, 1993, **32**(11), 2426–2432, DOI: 10.1021/ic00063a037.
88 K. Singh, S. Banerjee and A. K. Patra, *RSC Adv.*, 2015, **5**(130), 107503–107513, DOI: 10.1039/C5RA24329G.
89 Y. Inomata, T. Sunakawa and F. S. Howell, *J. Mol. Struct.*, 2003, **648**(1), 81–88, DOI: 10.1016/S0022-2860(02)00593-8.
90 V. Buzko, I. Sukhno and M. Buzko, *Int. J. Quantum Chem.*, 2007, **107**(13), 2353–2360, DOI: 10.1002/qua.21338.
91 M. S. Palmer, M. Neurock and M. M. Olken, *J. Phys. Chem. B*, 2002, **106**(25), 6543–6547, DOI: 10.1021/jp020492x.
92 N. Qureshi, D. Yufit, K. Steed, J. Howard and J. Steed, *CrystEngComm*, 2016, **18**, 5333–5337, DOI: 10.1039/C6CE01039C.
93 J. J. Dannenberg, *J. Am. Chem. Soc.*, 1998, **120**(22), 5604–5604, DOI: 10.1021/ja9756331.
94 V. Vennelakanti, H. W. Qi, R. Mehmood and H. J. Kulik, *Chem. Sci.*, 2021, **12**(3), 1147–1162, DOI: 10.1039/D0SC05084A.
95 W. F. Coleman, *J. Chem. Educ.*, 2008, **85**(9), 1296, DOI: 10.1021/ed085p1296.
96 K. Matsumoto, T. Tsuda, T. Nohira, R. Hagiwara, Y. Ito and O. Tamada, *Acta Crystallogr., Sect. C: Cryst. Struct. Commun.*, 2002, **58**(3), m186–m187, DOI: 10.1107/S0108270101020601.
97 Y. Han, C. Lin, Q. Meng, F. Dai, A. G. Sykes, M. T. Berry and P. S. May, *Inorg. Chem.*, 2014, **53**(11), 5494–5501, DOI: 10.1021/ic500101x.
98 G. Štefanić, S. Krehula and I. Štefanić, *Chem. Commun.*, 2013, **49**(81), 9245–9247, DOI: 10.1039/C3CC44803G.
99 P. R. Kumar, T. M. Maharajan, M. Chinnasamy, A. P. Prabu, J. A. Suthagar and K. S. Kumar, *Pharma Innovation J.*, 2019, **8**(5), 759–763.
100 P. S. Kohli, M. Kumar, K. K. Raina and M. L. Singla, *J. Mater. Sci.: Mater. Electron.*, 2012, **23**, 2257–2263, DOI: 10.1007/s10854-012-0793-7.
101 (*a*) CCDC 2491564: Experimental Crystal Structure Determination, 2025, DOI: 10.5517/ccdc.csd.cc2pmp12; (*b*) CCDC 2491565: Experimental Crystal Structure Determination, 2025, DOI: 10.5517/ccdc.csd.cc2pmp23.